Strain Localization Processes in Polymineralic Rocks: Insights from the Santa Rosa Mylonite Zone (CA)

By

Autumn Karalea Arnold

A Thesis Submitted to the Graduate Faculty of Auburn University in partial fulfillment of the requirements for the Degree of Master of Science in Geology

Auburn, Alabama

May 2, 2026

Approved by

Dr. Raphaël Gottardi (Chair), Associate Professor, Department of Geosciences

Dr. Brian Boston, Associate Professor, Department of Geosciences

Dr. Laura Bilenker, Associate Professor, Department of Geosciences

Abstract

Strain localization in ductile shear zones is a fundamental process governing the mechanical behavior of the lithosphere, yet the relative roles of mineralogical heterogeneity and microstructural evolution remain incompletely understood. This study investigates strain localization processes in the Santa Rosa mylonite zone (SRMZ), southern California, where deformation is heterogeneously distributed over centimeter scales, ranging from weakly deformed protoliths to ultramylonites. We integrate field observations with optical petrography, scanning electron microscopy (SEM-EDS), and electron backscatter diffraction (EBSD) to characterize microstructures, mineral chemistry, and crystallographic preferred orientations across proto-, meso-, and ultra- mylonitic rocks derived from a granodioritic protolith.

Quartz deformation is dominated by grain boundary migration recrystallization, with minor subgrain rotation, and exhibits c-axis fabrics indicative of prism <a> and subordinate rhomb <a> slip, consistent with deformation temperatures exceeding ~500 °C and a significant coaxial strain component. Feldspar records mixed brittle–ductile behavior, including fracturing, core-and-mantle structures, and limited recrystallization, while biotite defines the mylonitic foliation and develops S–C fabrics, locally forming mica fish and undergoing partial chloritization.

Our results demonstrate that strain is preferentially localized in quartz- and biotite-rich domains, where reduced aggregate strength and enhanced phase connectivity promote distributed deformation. In contrast, feldspar-rich domains tend to preserve a load-bearing framework, inhibiting strain localization. These observations indicate that primary mineralogical heterogeneity exerts a first-order control on strain partitioning, even under broadly uniform temperature and stress conditions. This study highlights the importance of mineralogy and phase distribution in governing shear zone initiation and development and provides new insights into the rheological evolution of mid-crustal deformation zones.

Artificial Intelligence (AI) Use Disclosure

In the preparation of this thesis, no Artificial Intelligence (AI) tools were used.

Digital Accessibility Use Disclosure Statement

In the preparation of this thesis, the following digital accessibility tools were used to ensure this document complies with federal requirements: Microsoft Office suite and Adobe Creative Cloud. The author acknowledges full responsibility for the intellectual content of this work and has made a good faith effort to comply with digital accessibility requirements in publishing, wherein the nature of the content does not significantly change in order to do so. Furthermore, all content has been reviewed and revised to meet these requirements prior to final publication.

Acknowledgements

I would like to thank my advisor Raphael Gottardi for encouraging me and providing guidance during the course of this project. Additionally, I also want to thank Dr. Laura Bilenker and Dr. Brian Boston for taking the time to give me feedback on my progress.

I thank Trey Adams and Niya Davis for helping me collect my field samples in the spring of 2025 and the rest of my cohort for their support during this time.

I would like to thank Auburn's GAB, GSA, and the Auburn Department of Geosciences for providing me with funds to attend my first conferences ever this past year.

Finally, I want to give thanks to my mother, brother, and grandparents, for always being there for me over the past two years; being on the phone with me listening to my excitement, stress, drama, and always supporting me through it all.

I would like to dedicate this thesis to Maddy, Chester, and Josephine, gone far too soon but never, ever forgotten.

Table of Contents

List of Tables

List of Figures

1. Introduction

1.1. Shear zones and Strain Accommodation

Strain in the crust and mantle is typically concentrated in shear zones, areas of intense deformation occurring from hand sample to regional scale structures (Fossen and Cavalcante, 2017). Studying shear zone initiation, development, and accompanying strain localization processes is critical to understanding the rheological response of crustal rocks (Gardner et al., 2017). In the cool upper crust, ~100°-300°C, strain is accommodated by brittle deformation mechanisms (fracturing, frictional sliding, grain rotation) resulting in the formation of fault gouge, breccia, and cataclasite (Figure 1).

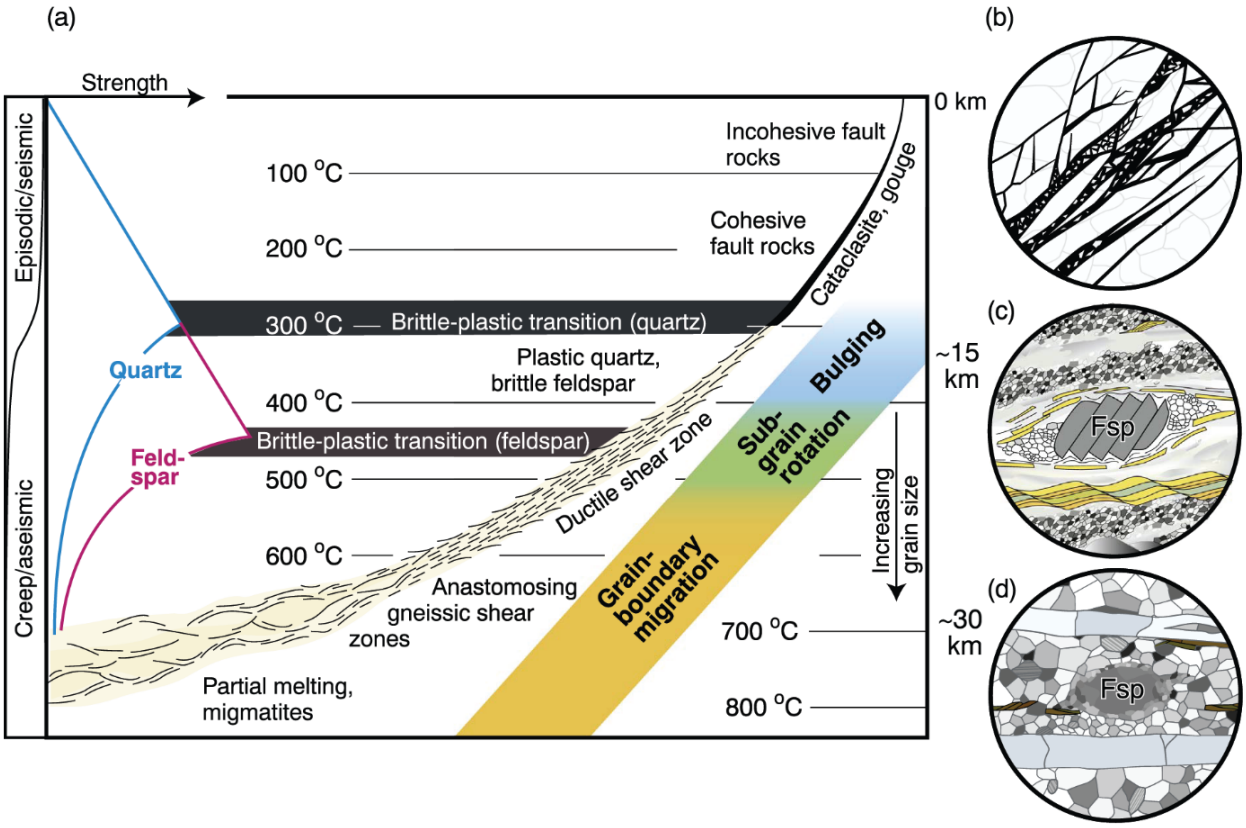

Figure 1. From Fossen and Cavalcante (2017). a) Simplified diagram of a crustal shear zone. The brittle-plastic transitions for quartz and feldspar and dominant recrystallization mechanisms (bulging, subgrain rotation and grain-boundary migration) are related to temperature but also depend on strain rate and the amount of fluids present. b–d) Illustration of characteristic microfabrics in the three different regimes: b) brittle fracturing (brittle mechanisms); c) plastic with brittle feldspar (central grain) and small recrystallized quartz grains (dislocation creep); d) high-temperature recrystallization where both feldspar and quartz behave plastically and grain-boundary migration by diffusion is significant.

Increasing depth and temperature, strain in the ductile middle to lower crust is accommodated by crystal-plastic deformation mechanisms (slip, twinning, creep) which are controlled by mineralogy and grain size of the host rock, temperature and pressure, fluid activity, strain rate, and rock heterogeneity (e.g., Kohlstedt et al., 1995) (Figure 1). Heterogeneity results from the strength contrast between the various minerals present, the volume fraction, connectivity, and geometric arrangement of weak minerals (e.g., phyllosilicates), the pre-existing fabrics (e.g., foliation) and the dominant deformation mechanisms in each mineral phase (see Gardner et al. 2017, and references therein). Field observations, experimental deformation work, and numerical modeling all indicate a wide range of strain localization patterns in ductile shear zones; from single zones of ultramylonite to anastomosing networks of high strain zones (e.g. Carreras et al., 2010; Gardner et al., 2017; Alaoui et al., 2023; Bui et al., 2023; Johnston et al., 2025; Li and Cao, 2025).

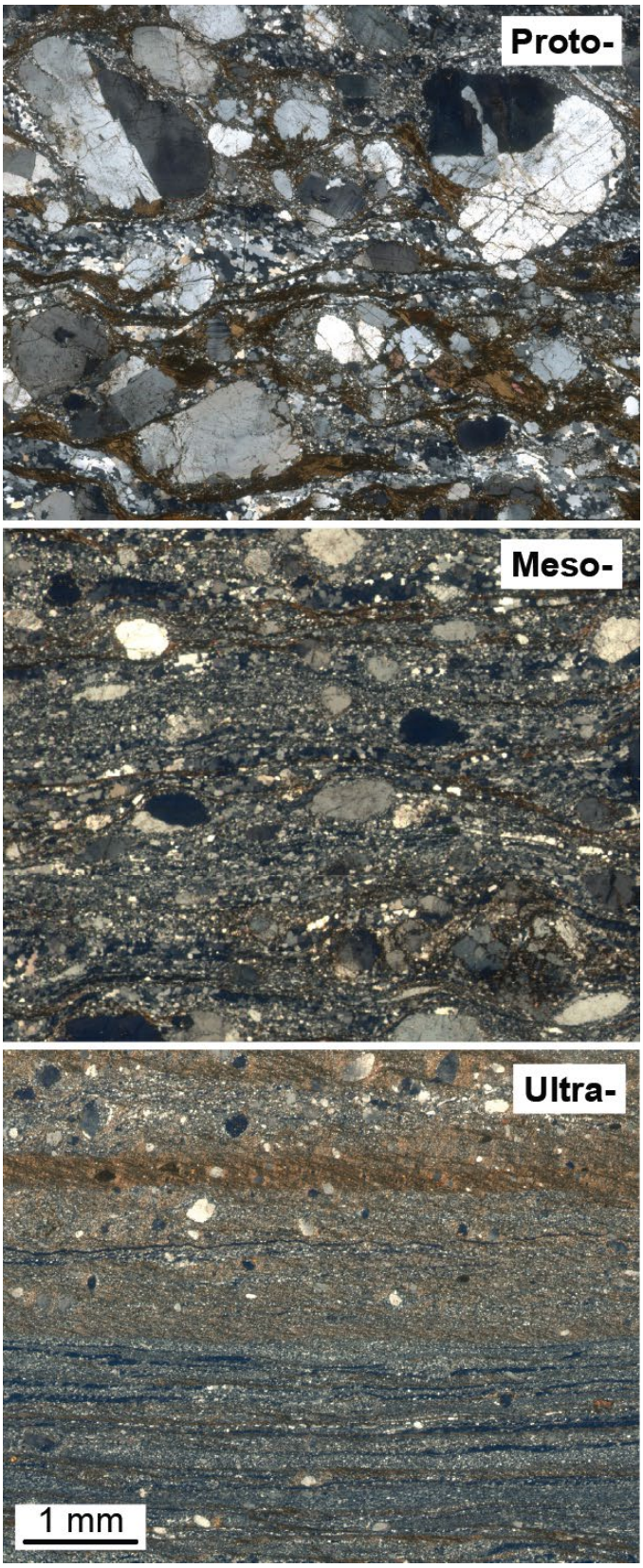

Figure 2: Photomicrographs of proto-, meso-, and ultra- mylonite fabrics.

1.2. Mylonite, Phyllonite, and Pseudotachylyte Presence and Classification

Mylonites are rocks indicative of areas in the earth's crust that have experienced relatively high grades of deformation and are often found in ductile shear zones; the term solely refers to rock texture and does not imply the presence of any specific mineral assemblages (Passchier and Trouw, 2005). There are three main types: *proto-*, *meso-*, and *ultra-* mylonite, all of which are classified based on the ratio of porphyroclasts to matrix, and total amount of recrystallized matrix (e.g., Figure 2) (Passchier and Trouw, 2005; Fossen, 2016). In the early stages of mylonitization, *protomylonites* typically contain more than 50% of porphyroclasts, and exhibit a weak but coarse foliation with minimal matrix recrystallization (< 25%). A *mesomylonite*, referred to by some simply as *mylonite*, contains only 10-50% porphyroclasts, is characterized by a well-developed foliation, and has undergone significant recrystallization yielding a grain size reduction of ≥ 50% of the matrix volume. Finally, an *ultramylonite* has small porphyroclasts remaining (< 10% of the matrix), is strongly foliated, and experienced extreme grain size reduction through dynamic recrystallization (≥ 90% of the matrix volume), giving the rock a dark, flint-like appearance.

Phyllonites (resembling phyllite) are cohesive, foliated phyllosilicate-rich fault rocks (e.g., Jeffries et al., 2006) which have been used to describe fine-grained mica-rich mylonites. *Pseudotachylytes* are rocks that have formed by local melting due to frictional heating of a rock along a brittle fault plane (e.g., Passchier and Trouw, 2005). They are typically characterized by a dark, aphanitic texture, with randomly oriented broken fragments of the host rock within them. These rocks, *phyllonite* and *pseudotachylyte*, are often used in place of *ultramylonite* due to their resemblance (overall dark color and fine grain size) in the field. Both rocks, however, are independent from each other and that of an ultramylonite.

1.3. Research Outcomes

The Santa Rosa mylonite zone (SRMZ) was chosen for this study because of the significant textural variation occurring just centimeters apart (Figures 2 and 3). Additionally, the SRMZ has been described by previous authors as "one of the largest, most intensely deformed and best exposed mylonite zones," (O'Brien et al., 1987). It is our view that the SRMZ is a great natural laboratory to examine strain localization mechanisms and an ideal location to delve into the heterogeneities of strain distribution in crustal rocks.

Ductile shear zones are controlled by the interactions of numerous overlapping parameters making them remarkably complex structures. Here, we focus on the influence mineralogy and rock heterogeneity has on strain localization, accommodation, and partitioning in the SRMZ; we also apply these findings to the greater implications of timing of exhumation and temperature of deformation in the SRMZ. The overarching aim of the study is to increase the collective knowledge of the mechanics of strain localization processes in ductile shear zones.

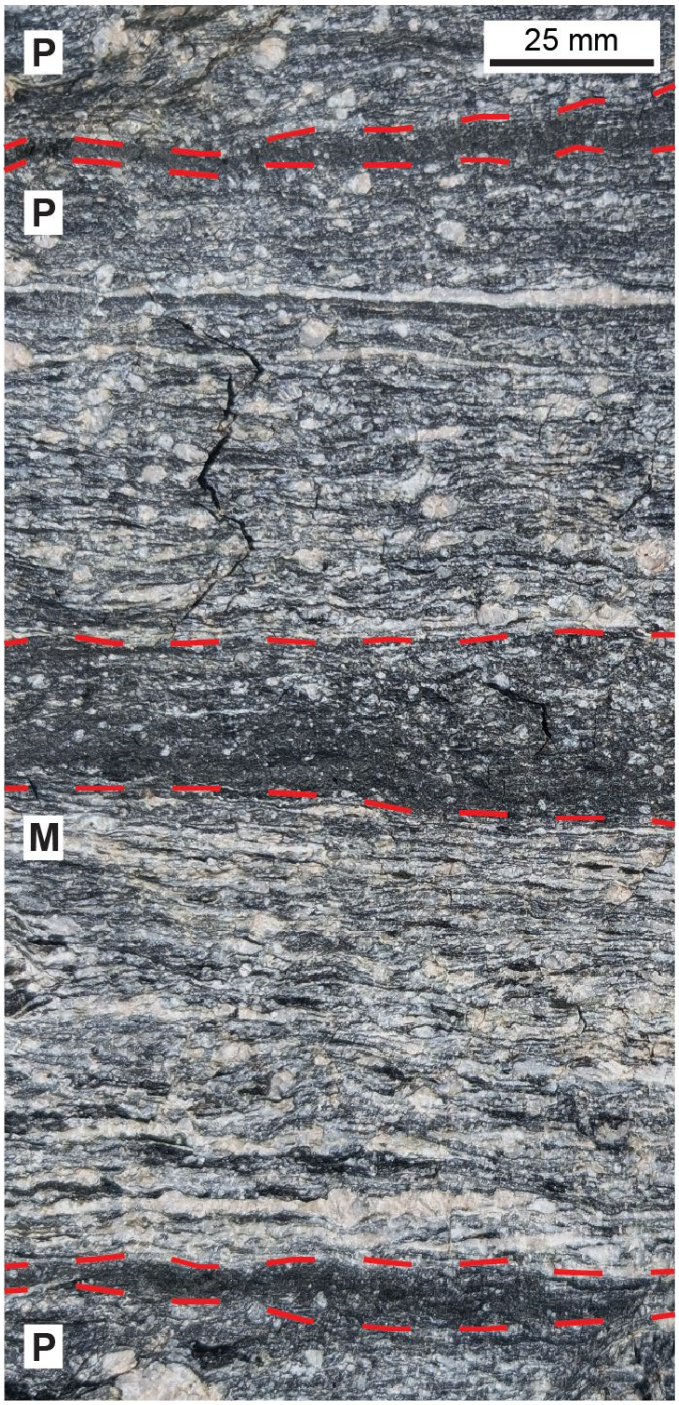

Figure 3: Varying degrees of mylonitization in the SRMZ; showing proximity of protomylonite (P), mesomylonite (M), and ultramylonite outlined with red dashes.

2. Regional Geology of the Santa Rosa Mylonite Zone

The Peninsular Ranges of southern California (Figure 4) is late Cretaceous in age (80–100 Ma) and formed as the result of the eastward subduction of the Farallon Plate (Jiang et al., 2015; Klepeis, 2025). The Peninsular Ranges hosts the Peninsular Ranges Batholith (PRB) of which there are two sides differing in composition, owed to the flat slab subduction of the Farallon Plate (~90 Ma). There is the mafic to felsic Western Peninsular Ranges (WPR) and the intermediate to felsic Eastern Peninsular Ranges (EPR) (Jones et al., 2025). The WPR and EPR are separated by low angle east-dipping faults which also distinguish the Asbestos Mountain granodiorite (~62 Ma, Goodwin and Renne, 1991) from the PRB. The EPR contains the Eastern Peninsular Ranges shear zone which hosts ~100 km of deformed rocks (Simpson, 1984). In this study, we focus on an 800 m thick sequence of granodioritic mylonites in the northern portion of the EPR shear zone known as the SRMZ (e.g., Erskine and Wenk, 1985; Wenk and Pannetier, 1990; Wenk, 1998).

Earlier studies place the formation of the SRMZ in the late Cretaceous and suggest it to be the result of the emplacement of the partially solidified PRB (97 Ma zircon U-Pb age Wenk, 1998) and its subsequent deformation (89 Ma from K-Ar cooling ages of cataclastic biotite, Goodwin and Renne, 1991). However, strict timing remains up for debate.

A significant amount of work has been conducted to investigate the mode of deformation that resulted in the SRMZ; if the deformation was predominantly coaxial “pure shear” or noncoaxial “simple shear” (e.g., Simpson, 1984; Erskine and Wenk, 1985). O’Brien et al. (1987) found evidence supporting Simpson (1984), that noncoaxial deformation took control. However, later Wenk (1998) investigated strain heterogeneity across the shear zone by analyzing xenolith orientations within the mylonites, revealing that they underwent ductile deformation via flattening in the xenolith geometry and that strain varied spatially across the field site. This supports that flattening occurred due to the emplacement of a partially solidified granodioritic batholith which then began to metamorphose the system.

The rocks found in and adjacent to the SRMZ are complex and have been documented by numerous researchers. Goodwin and Wenk (1995) reported that ultramylonites in the area are

"exceptionally rare", and synonymous with phyllonites in the SRMZ. Other papers have suggested that ultramylonite are instead recrystallized pseudotachylytes (Wenk et al., 2000). However, although pseudotachylyte abundant and well-studied in the overlying Palm Canyon Complex (Wenk et al., 2000; Ferré et al., 2012; Rowe et al., 2012), they have never been documented in the SRMZ. Goodwin and Wenk (1995) noted that in the SRMZ, phyllonite and ultramylonite are very similar. Both are dark in color, gray to black and 'aphanitic'/'massive', but the former resembled slate, was slightly browner, cleaved along foliation planes, and had a micaceous sheen. The latter lacked those characteristics. Bulk chemical and mineralogic analyses by X-ray fluorescence and powder diffraction showed nearly identical composition for these two rocks (Goodwin and Wenk, 1995).

Wenk and Pannetier (1990) generally traced granodioritic protoliths of the PRB to their deformed counterparts and found the transition between them to be rather abrupt. They investigated micro- textures and structures from the granodiorites to examine how deformation is reflected on the mineral assemblage of biotite, quartz, and plagioclase. They found strong crystallographic preferred orientations (CPO's) had developed in biotite and quartz but were lacking in plagioclases. However, despite this, they observed mineral phases are not readily changed; quartz, plagioclase, and biotite, remained recognizable in the deformed proto- to ultra-mylonitic rocks.

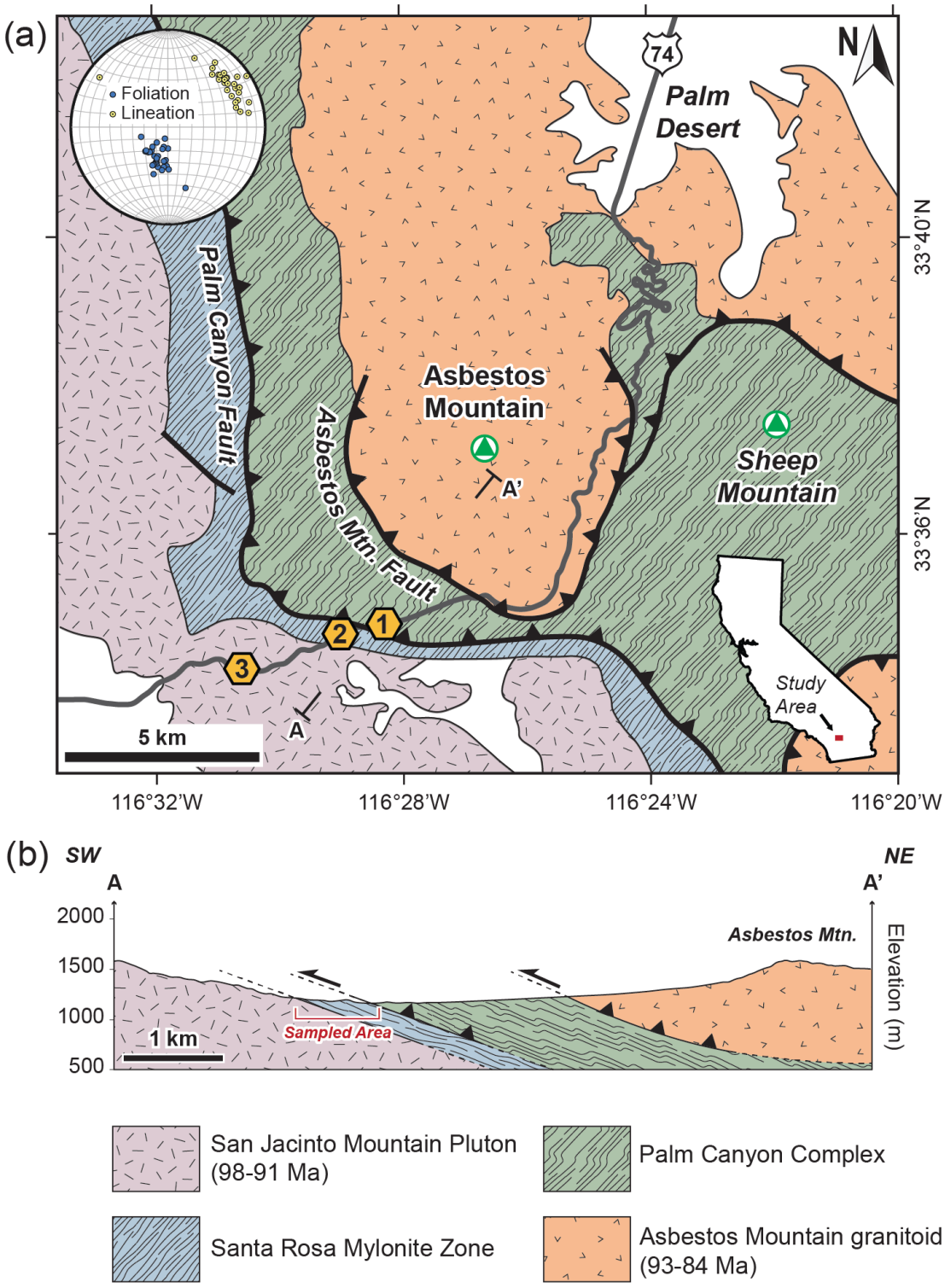

Figure 4: Map modified from Jiang et al (2015). (a) Structural map displaying sample collection sites 1, 2, and 3 in orange hexagons (mylonites collected from sites 1 and 2, protoliths collected from site 3); top left shows stereonet plotting foliation (SW) and lineation (NE) of collected samples from locales 1 and 2; bottom right shows location of research site in southern California. (b) Cross-section of structural map at transect A-A', thrusting to the SW; red brackets show sample collection units.

3. Methods

To achieve the project objectives, we combined field measurements and observations with standard optical microscopy and scanning electron microscopy (SEM) methods, including energy dispersive spectroscopy (EDS) and electron backscatter diffraction (EBSD). These methods were used to characterize the fabric of the samples and the major element chemistry of the dominant mineral phases. Comparing field notes with micro- structural/textural features, allowed us to identify the deformation mechanisms that have taken place at the microscale and additionally verify the overall mineralogy of the samples.

3.1. Field Measurements and Sample Collection

Field work was conducted in March 2025 at three locations. Deformed rocks were collected from two locations and protoliths were collected from the third, noted in Figure 4. At each location, investigative transects were conducted perpendicular to the foliation in order to observe any fabric changes with structural depth. Field relationships, basic fabric intensity (proto-, meso-, and ultra-mylonitic), and sample orientation (foliation and lineation) were recorded in the FieldMove Clino Application and verified with a Standard Transit Brunton Compass. The main goal of this

field work was to document the in-situ orientation and collect samples of varying mylonitic fabrics.

Figure 5: Left: FieldMove Clino application used to record field observations and verified in image on right with Standard Transit Brunton Compass.

3.2. Optical Petrography

All 35 samples collected in the field were cut and analyzed to identify the best representative samples of proto-, meso-, and ultramylonitic textures observed. Of the 35 samples, 30 billets were sent to Spectrum Petrographics Inc. to prepare standard petrographic thin sections. These thin sections were used to conduct our microstructural analysis using standard optical microscopy. Three representative samples total were chosen to represent protomylonitic texture (PC25-04), mesomylonitic texture (PC25-06), and ultramylonitic texture (PC25-30). The main objective of optical microscopy was to identify the dominant deformation mechanisms in the major mineral phases present in the samples: quartz, plagioclase, and biotite.

3.3. Scanning Electron Microscopy (SEM) Energy Dispersive Spectroscopy (EDS)

EDS was used to semi-quantitatively characterize the major element chemistry of feldspar, plagioclase, biotite, and other minerals present in thin section of each of the representative samples: PC25-04, PC25-06, PC25-30. Major element chemistry of the mylonitic rocks was compared to the undeformed samples in an attempt to identify the protolith. Additionally, EDS

was used to identify mineral phases that were challenging to identify on the petrographic microscope (e.g., K-feldspar vs. plagioclase).

Polished thin sections were first coated in 5 nm carbon using a JOEL EC-32010CC carbon coater. Backscattered electron (BSE) and EDS data were then collected using a Zeiss EVO 15 SEM operated in high vacuum mode and equipped with a 65 mm^2 Oxford Ulti Max energy dispersive spectroscopy (EDS)-silicon drift detector operating with Oxford Aztec software. Typical operating conditions for imaging were a 20 keV accelerating voltage and 1-8 nA of beam current.

3.4. SEM EBSD

EBSD was used to investigate the crystallographic fabric of the samples PC25-04, PC25-06, and PC25-30, primarily to measure the crystallographic preferred orientation (CPO) of quartz and produce grain boundary maps in order to characterize the grain size(s) of each sample. CPO can be used to infer temperature of deformation as well as kinematics (pure vs. simple shear). Recrystallized grain size is stress sensitive, and paleopiezometers can be used to infer differential stress from recrystallized grain size (e.g., Stipp et al, 2003; Cross et al., 2017). Flow laws, differential stress and temperature estimates can be used to constrain the strain rate experienced by the mylonites (e.g., Hirth et al, 2001). Finally, since the recrystallized grain size in mylonites can be very small (micron scale) mineral identification is challenging on a regular microscope (e.g. quartz vs. plagioclase) EBSD can be used to distinguish between different crystalline phases.

EBSD data were collected on the same Zeiss EVO 15 SEM using 20 kV accelerating voltage and 20 to 60 nA beam current. EBSD patterns were collected on an Oxford AZtecHKL EBSD C-Nano and processed and indexed using Oxford Instruments AZtec software. Each sample was mapped at step sizes ranging from 4 to 6 μm.

4. Results

4.1. Field Observations

Twenty-nine mylonite samples were collected: 16 samples at Location 1 and 13 samples at Location 2. Additionally, six samples of the undeformed protolith were collected at Location 3, for a total of 35 samples overall (Figure 4 ; Table 1). Deformed xenoliths (Figure 6a) were abundant in the SRMZ, as previously recorded by Wenk (1998) along with various amounts of microfolds (e.g., sheath folds; Figure 6b). Strikingly, however, we came across a plethora of lenses of seemingly undeformed material that resembling amphibole in the field (Figure 6c). The proximity of these completely opposing structures remains puzzling.

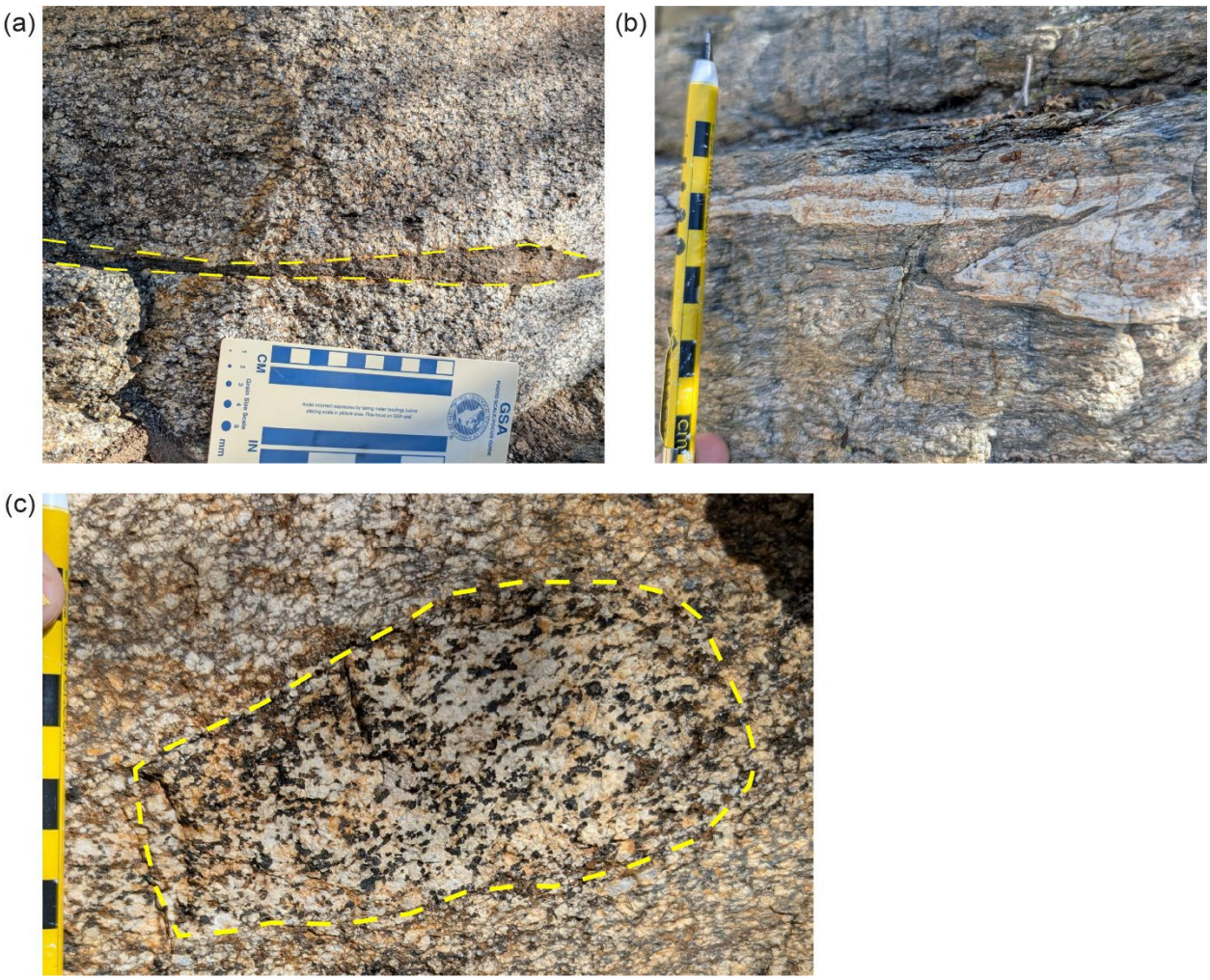

Figure 6: (a) Stretched xenolith outlined in dashed yellow lines. (b) Feldspar sheath fold between high grade layers. (c) Undeformed 'sandwich' of biotite and amphibole.

Table 1. Sample name, fabric, location, foliation, and lineation of all collected samples.

Sample	Fabric	Latitude, Longitude	Fol: strike/dip	Lin: plunge→trend
PC25-01	Proto-	33°34’44” N, 116°28’05” W	290°/28°	25°→054°
PC25-03	Proto-	33°34’44” N, 116°28’05” W	289°/26°	20°→064°
PC25-04	Proto-	33°34’44” N, 116°28’05” W	N/A	25°→021°
PC25-06	Meso-	33°34’44” N, 116°28’05” W	292°/35°	27°→070°
PC25-09	Meso-	33°34’44” N, 116°28’05” W	313°/28°	28°→074°
PC25-12A	Meso-	33°34’44” N, 116°28’08” W	291°/34°	28°→064°
PC25-12B	Meso-	33°34’44” N, 116°28’08” W	291°/34°	28°→064°
PC25-14A	Ultra-	33°34’44” N, 116°28’08” W	284°/19°	19°→036°
PC25-14B	Ultra-	33°34’44” N, 116°28’08” W	284°/19°	19°→036°
PC25-15	Ultra-	33°34’44” N, 116°28’08” W	276°/34°	23°→050°
PC25-17	Meso-	33°34’44” N, 116°28’08” W	282°/17°	13°→054°
PC25-19	Meso-	33°34’44” N, 116°28'12" W	N/A	04°→057°
PC25-20	Meso-	33°34’41” N, 116°28'12" W	274°/28°	22°→050°
PC25-21	Meso-	33°34’41” N, 116°28'12" W	306°/26°	24°→046°
PC25-22	Meso-	33°34’41” N, 116°28'12" W	289°/29°	25°→051°
PC25-23	Ultra-	33°34’34” N, 116°28'37" W	285°/10°	14°→306°
PC25-25	Ultra-	33°34’35” N, 116°28'37" W	305°/24°	29°→058°
PC25-26	Ultra-	33°34’35” N, 116°28'37" W	289°/31°	29°→047°
PC25-27	Ultra-	33°34’35” N, 116°28'37" W	254°/55°	27°→052°
PC25-28	Meso/Ultra-	33°34’36” N, 116°28'37" W	270°/18°	30°→040°
PC25-30	Ultra-	33°34’37” N, 116°28'36" W	308°/27°	27°→046°
PC25-31	Meso/Ultra-	33°34’37” N, 116°28'35" W	272°/33°	25°→037°
PC25-32	Ultra-	33°34’38” N, 116°28'35" W	284°/35°	26°→044°
PC25-CG1	Protolith	33°34’07” N, 116°30'48" W	Not oriented	
PC25-CG2	Protolith	33°34’07” N, 116°30'48" W	Not oriented	
PC25-FG1	Protolith	33°34’07” N, 116°30'48" W	Not oriented	
PC25-FG2	Protolith	33°34’07” N, 116°30'48" W	Not oriented	
PC25-AMP1	Protolith	33°34’07” N, 116°30'48" W	Not oriented	
PC25-AMP2	Protolith	33°34’07” N, 116°30'48" W	Not oriented	

4.2. Microstructural Analysis

4.2.1. Protomylonite: PC25-04

PC25-04 is a representative protomylonite sample composed of ~ 30% quartz, ~50% feldspars, and ~15% biotite, is weakly foliated (Figure 7a). Quartz typically occurs either in lenses of recrystallized grains subparallel to the mylonitic foliation, or as finely recrystallized grains intermixed with feldspar in the tails of larger feldspar porphyroclasts (Figures 7b, c). Quartz lenses show sub-equant grains with irregular but serrated boundaries and uniform size (~30-50 μm), characteristic of recrystallization by grain boundary migration (Regime III of Hirth and Tullis, 1992) (Figure 7b). In the tails of porphyroclasts, quartz is very finely recrystallized (< 10 μm) and intermixed with equally small size feldspar grains, making it difficult to distinguish the two on the petrographic microscope.

Feldspar grains range from 250 μm to several millimeters in diameter, typically form rigid augen-porphyroclasts with characteristic σ- and δ- shear sense indictors, and are consistent with a top-to-the-SW sense of shear (Figure 7c). Feldspar fragments show intracrystalline deformation including patchy undulose extinction and grain erosion is evident in areas of high stress (Figure 7d). Porphyroclasts show a mantle of finely grained feldspar with sharp boundaries around the core of the grain, forming typical core-and-mantle structures (Figures 7a, c, d). Such microstructures are indicative of recrystallization by bulging and by nucleation and growth of new grains, indicative of medium-grade conditions (450–600°C) deformation conditions (Passchier and Trouw, 2005). Myrmekitic texture occasionally occurs inside feldspar clasts that are adjacent to quartz, indicative of deformation-induced origin and typical for upper greenschist- to lower amphibolite-facies deformation conditions (Ceccato et al., 2018; Pryer, 1993; Simpson and Wintsch, 1989) (Figure 7e). Biotite dominantly occurs as fine-grained elongated clusters defining both S and C surfaces and occasionally surrounding feldspar porphyroclasts (Figures 7a, b, c, f). The biotite grains are mostly finely recrystallized and generally aligned with their [001] cleavage plane parallel to mylonitic foliation, rarely forming mica fish. (Figure 7f).

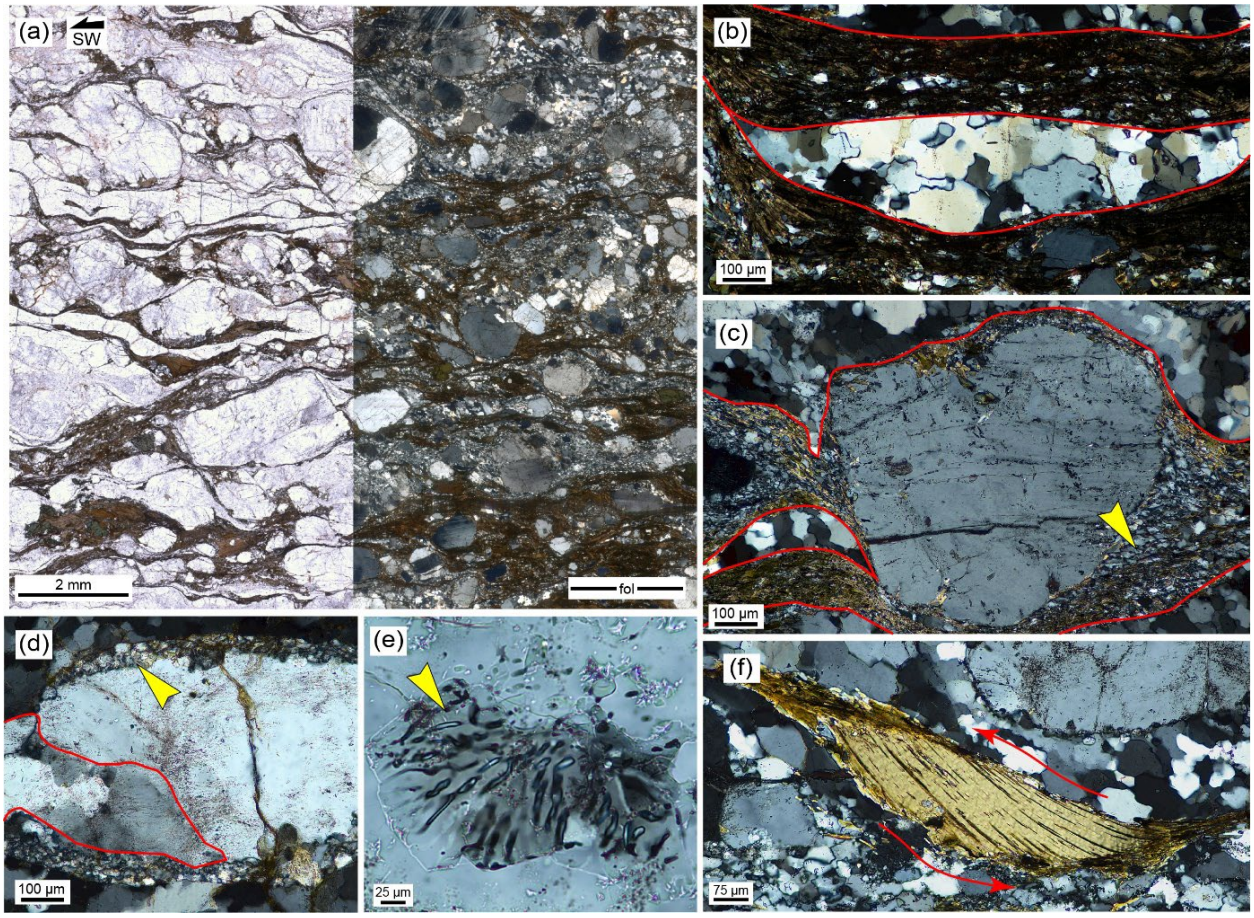

Figure 7: PC25-04 protomylonite textures observed in thin section. (a) Full scan of PC25-04 thin section with top left indicating shear sense, left is in plane polarized light, right is in crossed polarized light. (b) Biotite ribbons capturing a quartz lens outlined in red; recrystallized quartz via grain boundary migration. (c) Feldspar porphyroclast with quartz, outlined in red, in pressure shadows consisting of finely recrystallized quartz via GBM and feldspar. (d) Feldspar crystal showing undulose extinction (red outline), example of bulging recrystallization in feldspar (yellow arrow). (e) Myrmekitic texture in feldspar (yellow arrow). (f) Biotite mica fish showing sense of shear. Thin sections are cut oriented perpendicular to the foliation and parallel to the lineation, with a top left shear sense. All detailed photomicrographs are taken in crossed polarized light.

4.2.2. Mesomylonite: PC25-06

The mesomylonite sample appears to contain slightly more quartz (~ 35%) and biotite (~ 20%) and less feldspars (40%) than the protomylonite, with trace amounts of the same minerals (zircon, apatite, and titanite) and amphibole in some samples. The mylonitic foliation (C fabric) is well developed, expressed by layers of small biotite grains and thin bands (~50 – 150 μm) of recrystallized quartz (Figure 8a). Quartz dominantly occurs in thin layers (< 250 μm thick) of recrystallized grains subparallel to the mylonitic foliation (Figures 8a, b). The quartz microstructures are similar to that of the protomylonite: sub-equant grains exhibit irregular but serrated boundaries characteristic of recrystallization by grain boundary migration (Regime III of Hirth and Tullis, 1992). The quartz recrystallized grain size is also similar to the protomylonite (~30-50 μm). In the mesomylonite, bands of finely recrystallized quartz and feldspar are not restricted to the tails of feldspar porphyroclasts, but extend across the thin section, and can reach several mm in thickness (Figure 8a). In such bands, it is difficult to differentiate quartz from feldspar due to the small recrystallized grain size (< 10 μm). Most feldspar grains are fractured with associated rotation, bookshelf microstructures are common (Figure 8c). Feldspar grains form well-developed σ- and δ- augens consistent with a top-to-the-SW sense of shear (Figure 8d). Intracrystalline deformation of feldspar grains is indicated by undulose extinction and bent twins. Some feldspar grains exhibit tartan twinning characteristic of microcline. Myrmekitic texture occasionally occurs along grain margins oriented perpendicular to the maximum shortening direction and grain erosion in areas of high stress leads to the development of oval grains with characteristic core and mantle texture (Figures 8d, e). Bulging recrystallization of the feldspar is evident in nearly all augen-porphyroclasts (Figure 8e). Locally, biotite may be replaced by chlorite (Figure 8f), which has previously been reported in the area (Goodwin and Renne, 1991).

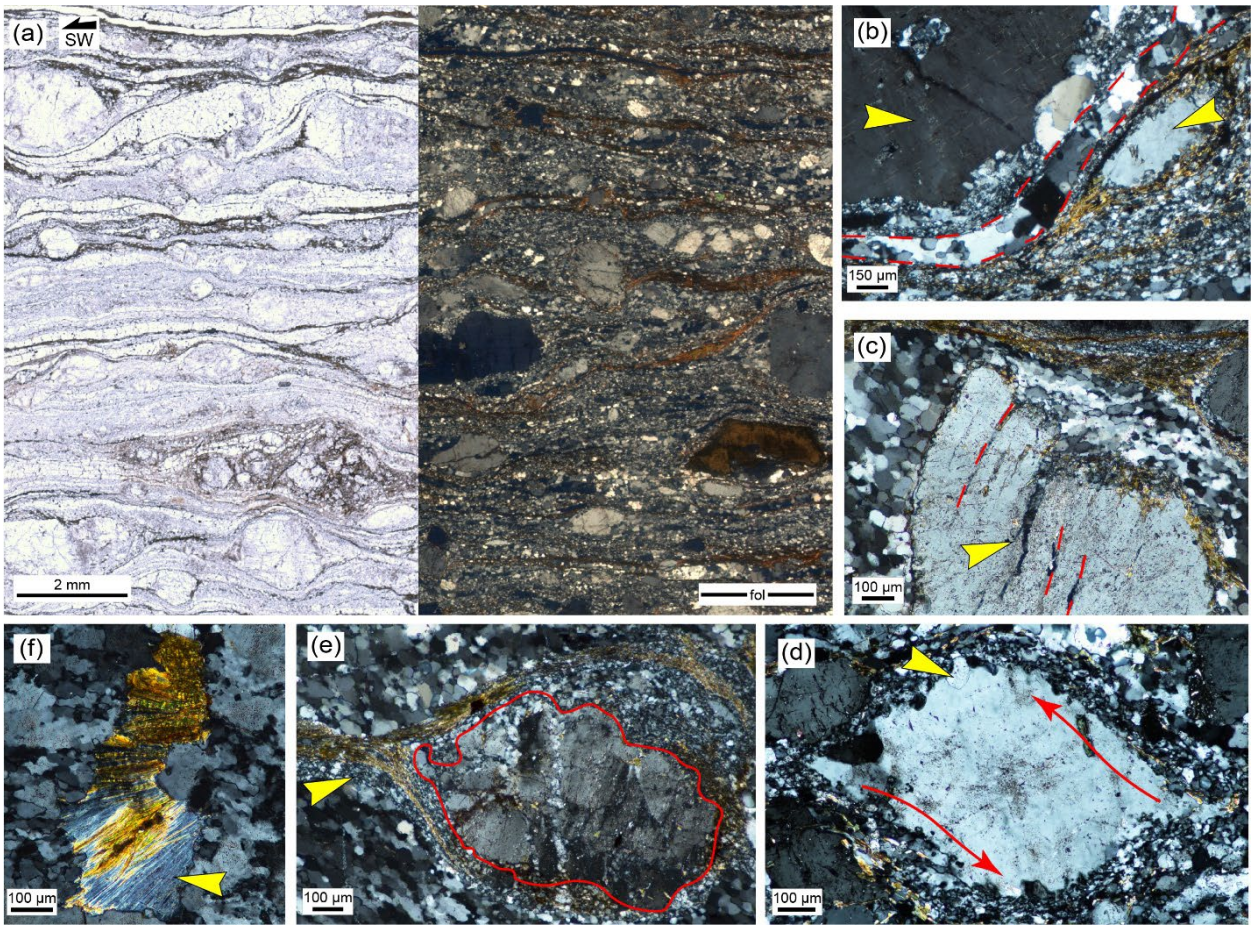

Figure 8: Representative microstructures of the mesomylonite textures, PC25-06. (a) Full scan of representative mesomylonite thin section with top left indicating shear sense, left image is in plane polarized light, right is in crossed polarized light. All photomicrographs are oriented with the same shear sense as full scan. (b) Feldspar porphyroclasts, yellow arrows, trapping quartz ribbon, red dashes. (c) Feldspar brittlely deforming, yellow arrow, along cleavage planes red dashes. (d) Core-and-mantle structure of feldspar porphyroclast showing SW sense of shear, red arrows, myrmekitic lobes are common around the edge of porphyroclasts, yellow arrow. (e) Relict feldspar porphyroclast, outlined in red, mantled by finely recrystallized quartz and feldspar, yellow arrow. (f) Chlorite, yellow arrow, replacing biotite. Thin sections are cut oriented perpendicular to the foliation and parallel to the lineation, with a top left shear sense. All detailed photomicrographs are taken in crossed polarized light.

4.2.3. Ultramylonite: PC25-30

The ultramylonite is nearly completely recrystallized, except for a few feldspar grains that form beautiful δ- and σ-type porphyroclasts indicating a top-to-the-SW sense of shear (Figure 9). In the ultramylonite samples, biotite seems more abundant (~30%) and is also very finely recrystallized. The foliation is well-developed, although can be wavy in some samples (e.g., Figure 9a). The ultramylonite shows a texture with alternating domains of recrystallized quartz/feldspar and biotite. In the biotite rich domains, the biotite expresses the typical S-C fabric (Figure 9b).

Quartz occurs locally in thin bands (< 100 μm thick) parallel to the foliation, deformation mechanisms seem to be similar to that of the proto- and meso-mylonite. Recrystallized grains have irregular but serrated boundaries characteristic of recrystallization by grain boundary migration (Figure 9c; Regime III of Hirth and Tullis, 1992). The recrystallized grains tend to define a secondary oblique foliation consistent with the top to the southwest shear sense. Few quartz relic grains (i.e., non-fully recrystallized grains) exhibit undulose extinction. The recrystallized grain size is very fine (< 20 μm) making it difficult to distinguish feldspar from quartz (Figures 9c, d).

Nearly all large feldspar grains exhibit evidence of brittle intracrystalline deformation (Figures 9d, e). Feldspar porphyroclasts have experienced grain size reduction by grain erosion. Bulging recrystallization of the feldspar affects most augen-porphyroclasts leading to characteristic core and mantle texture (Figure 9d, e).

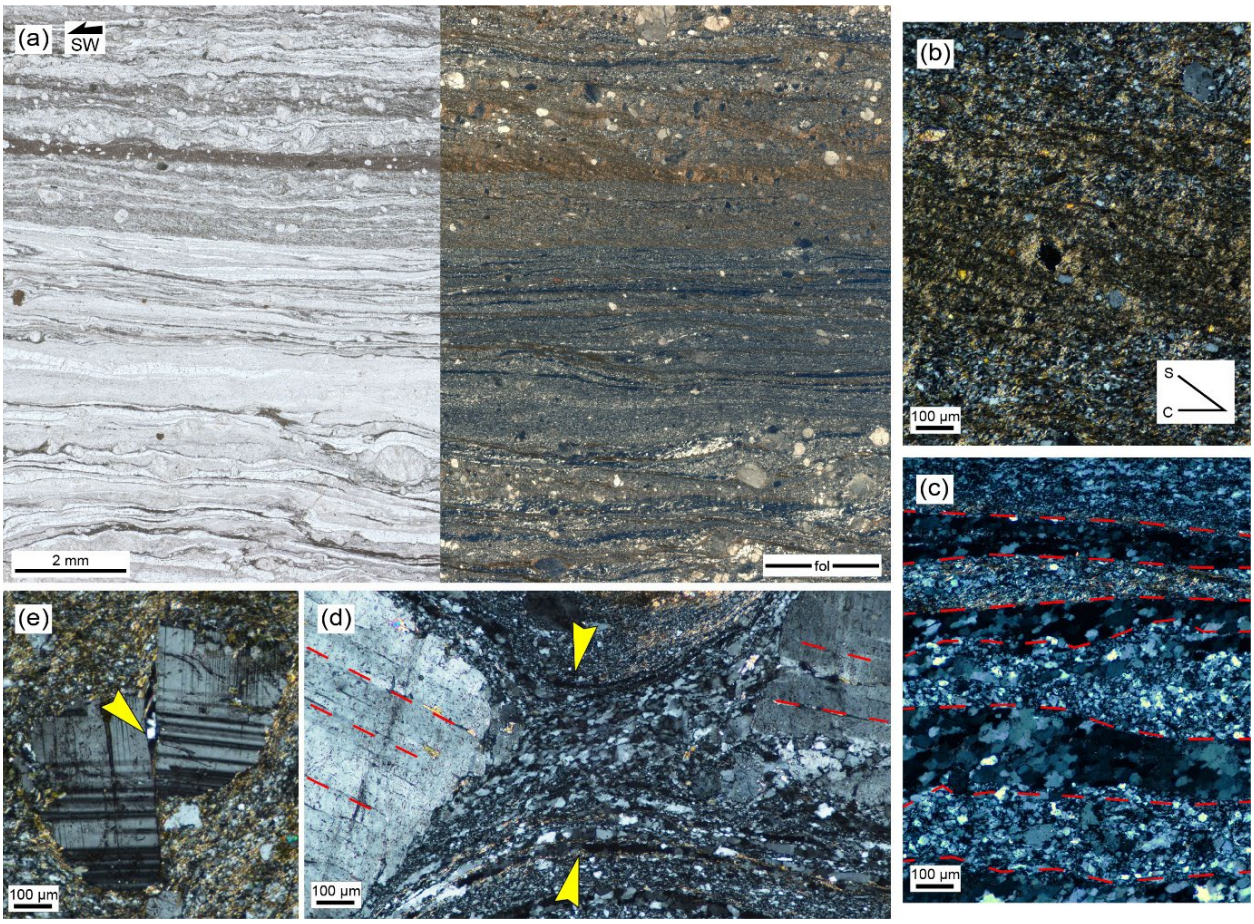

Figure 9: Representative microstructures of the ultramylonite textures from PC25-30. (a) Full scan of representative ultramylonite thin section with top left indicating shear sense, left image is in plane polarized light, right is in crossed polarized light. (b) S-C texture is well-developed in the biotite rich domains. (c) Outlined in red are bands of dark, finely recrystallized quartz grains deformed by GBM recrystallization, and very fine recrystallized feldspars. (d) Finely recrystallized quartz and feldspar, yellow arrows, in the tails of large feldspar porphyroclasts that are deforming brittlely with cleavage planes marked by red dashes. (e) Yellow arrow denoting slip plane on fractured felspar grain. All photomicrographs are oriented with the same shear sense as full scan. Thin sections are cut oriented perpendicular to the foliation and parallel to the lineation, with a top left shear sense. All detailed photomicrographs are taken in crossed polarized light.

4.3. EDS Results

Our aim with EDS analysis was to link the mylonite samples PC25-04, PC25-06, and PC25-30, to their proper protolith: fine grained granodiorite, course grained granodiorite, or coarse grained tonalite. Additionally, we used EDS to characterize the major element chemistry of the dominant minerals found in the samples.

4.3.1. Protomylonite: PC25-04

Generally, the BSE imagery (Figure 10a) showcases elongated quartz ribbons (darkest gray), feldspar relict grains and finely recrystallized grains are disseminated throughout (medium gray). Exsolution in larger feldspar porphyroclasts can be seen by lighter gray patches. Biotite shows up as light gray in BSE, and accessory heavy minerals like zircon shows up the brightest gray (Figure 10a). The Si map is useful for characterizing quartz distribution and identifying recrystallized quartz from recrystallized feldspar in porphyroclast tails (Figure 10a). The Si map shows that quartz tend to form bands and swaths, where it is rarely mixed with feldspar. Porphyroclasts tails consist entirely of recrystallized feldspar (Figure 10a). Relict feldspar porphyroclasts show compositional variation between K, Na, and Ca (Figure 10c, d, e). K occurs near the center of relict grains (Figure 10c) as well as in pre-existing weaknesses in the mineral (i.e., cleavage planes) indicating initiation of alteration of plagioclase to K-feldspar. The feldspars overall are Na-rich (Figure 10d) some individual grains show moderate zoning in Ca (Figure 10e).

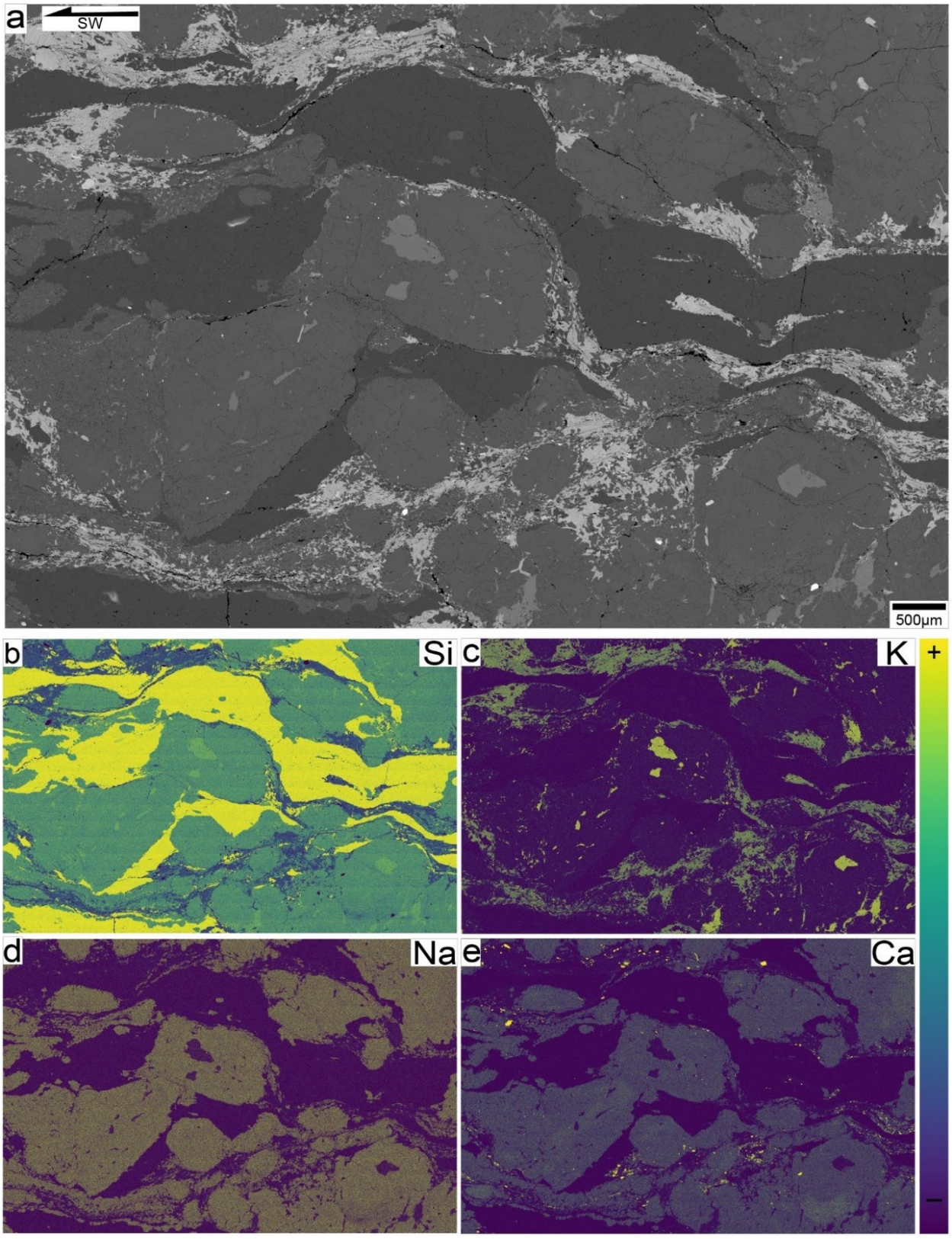

Figure 10: EDS results for protomylonite. (**a**) BSE image and Si (**b**), K (**c**), Na (**d**), and Ca (**e**) compositional maps.

4.3.2. Mesomylonite: PC25-06

BSE images nicely reveal mylonitic foliation in mesomylonitic sample PC25-06, expressed by bands of recrystallized quartz and feldspars (Figure 11a). Interestingly, contrary to what we observed in the protomylonitic samples, quartz and feldspar form bands of mixed composition in the mesomylonitic samples, giving a "peppered" look in BSE (Figure 11a, b). Feldspar porphyroclasts are primarily composed of Na (Figure 11d) and exhibit zoning of Ca (Figure 11e). Some porphyroclasts show an increase of K in their centers (Figure 11c) and are zoned with Na, indicating alteration. K-feldspar porphyroclasts retain less of their crystal habit and result in σ-type porphyroclasts (Figure 11c). Areas along cleavage planes and pressure shadows between porphyroclasts also show alteration from Na/Ca to K.

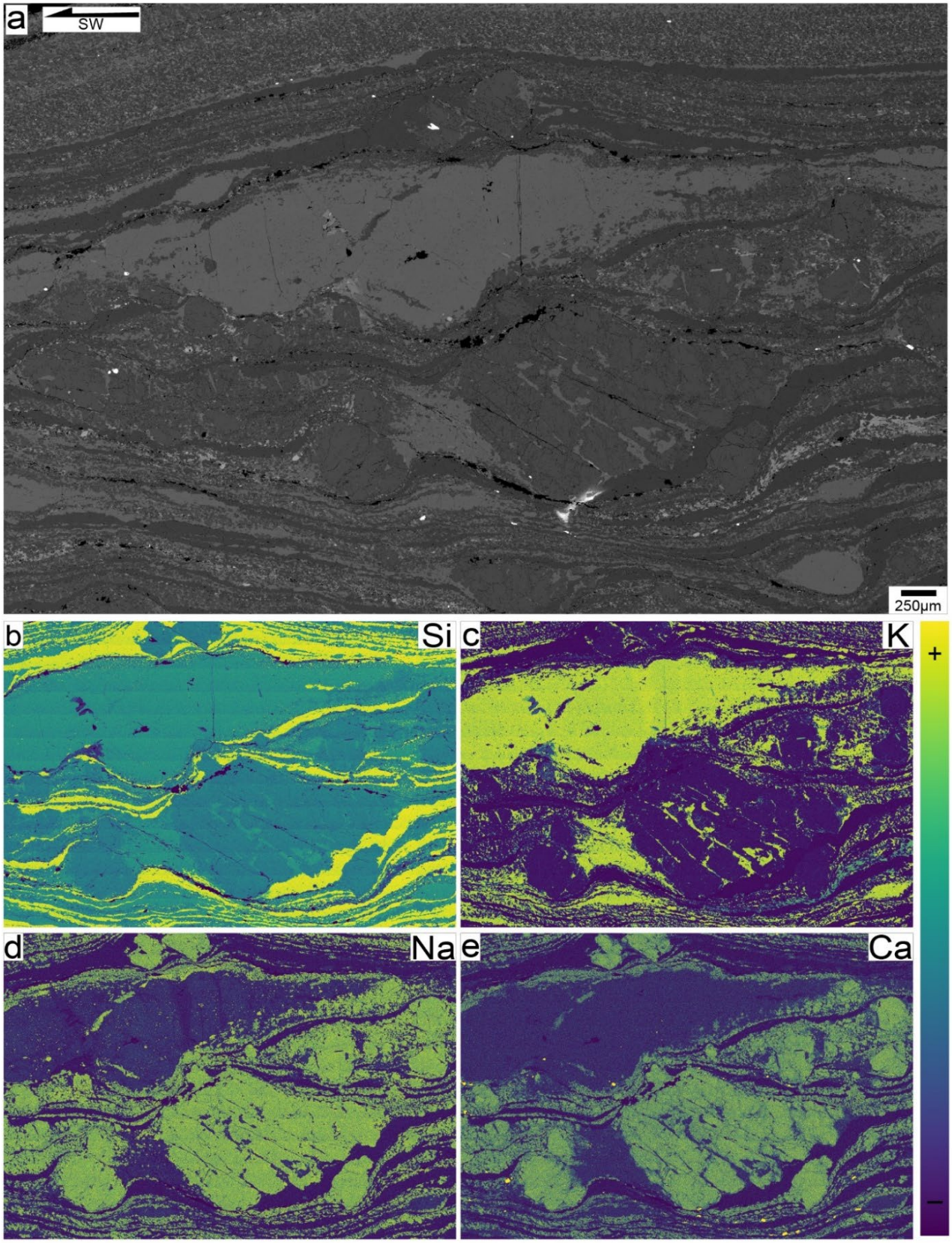

Figure 11: EDS results for protomylonite. (a) BSE image and Si (b), K (c), Na (d), and Ca (e) compositional maps.

4.3.3. Ultramylonite: PC25-30

For the ultramylonitic samples, we focused our EDS analysis on the quartz and feldspar rich domains. BSE image reveals that the mylonitic fabric is expressed by bands of different compositions: there are bands of pure quartz (Figure 12b), but also bands of intermixed quartz and feldspar (Figure 12d, e). Feldspar erosion led to porphyroclasts with elongated tails that stretched significantly along the lineation direction. Feldspar porphyroclasts here are also composed of a mixture of Na and Ca (Figure 12d, e). K occurs in the cleavage planes of porphyroclasts (Figure 12c) and in smaller porphyroclasts.

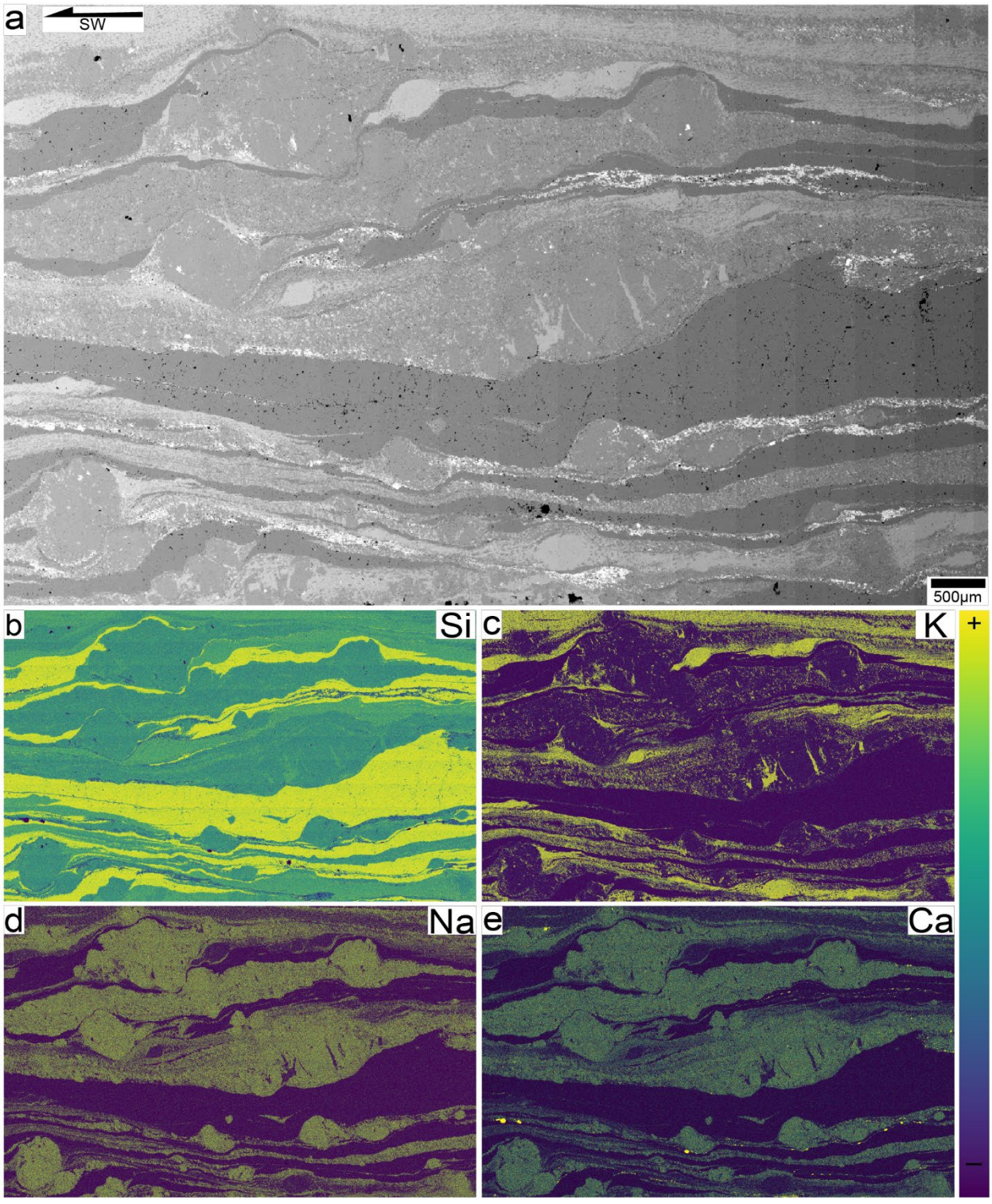

Figure 12: EDS results for ultramylonite. (a) BSE image and Si (b), K (c), Na (d), and Ca (e) compositional maps.

4.3.4. Semi-quantitative major element chemistry

SEM-EDS spot analyses were conducted on the dominant mineral assemblages, and representative composition is reported in Table 2. K-feldspars contain ~12 wt% K_2O, and < 1 wt% of Na_2O and CaO (Table 2). Combined with the observation of tartan twinning in some of the grains, we suggest that the K-feldspars are mostly microcline ($KAlSi_3O_8$). Analyzed plagioclase grains were relatively homogeneous in composition, with 5-6 wt% Na_2O and 5-6 wt% of CaO, suggesting a composition of ~ $An_{70}Ab_{30}$ consistent with labradorite (Table 2). Spot analyses of amphiboles indicate ~6 wt% MgO, ~10 wt% CaO, and ~20 wt% FeO, suggesting a ferro-actinolite composition (Table 2).

Table 2: Semi-quantitative major element chemistry (in wt.%) of the main mineral species obtained by SEM-EDS analyses.

	Protomylonite [PC25-04]	**Mesomylonite [PC25-06]**	**Ultramylonite [PC25-30]**
		K-feldspar	
SiO_2		50 ± 2	56 ± 2
Al_2O_3		14 ± 2	16 ± 1
MgO			
CaO			
MnO			
FeO			
Na_2O		< 1	< 1
K_2O		12 ± 1	15 ± 1
TiO_2			
		Plagioclase	
SiO_2	45 ± 4	46 ± 4	51 ± 2
Al_2O_3	16 ± 4	18 ± 2	21 ± 2
MgO			
CaO	5 ± 2	5 ± 2	6 ± 1
MnO			
FeO	< 1		
Na_2O	5 ± 1	6 ± 1	6 ± 1
K_2O	< 1	< 1	< 1
TiO_2			
		Biotite	
SiO_2	25 ± 2	25 ± 2	21 ± 2
Al_2O_3	11 ± 1	12 ± 1	15 ± 1
MgO		5 ± 1	6 ± 1
CaO	< 1		
MnO		< 1	< 1
FeO	16 ± 1	18 ± 1	21 ± 1
Na_2O	< 1		
K_2O	6 ± 1	7 ± 1	8 ± 1
TiO_2		3 ± 1	3 ± 1
		Amphibole	
SiO_2	28 ± 4		36 ± 2
Al_2O_3	7 ± 1		9 ± 1
MgO			6 ± 1
CaO	9 ± 1		11 ± 1
MnO			< 1
FeO	18 ± 1		22 ± 1
Na_2O	< 2		< 1
K_2O	< 2		< 2
TiO_2			< 1

4.4. Quartz Crystallographic Orientation Results

Recrystallization mechanisms and the crystallographic preferred orientation (CPO) of quartz determined by SEM EBSD revealed that quartz deformation is accommodated by dislocation creep processes, and recrystallized grains exhibit a strong CPO (Figure 13). Quartz c-axis fabrics display a typical Type-I cross-gridle (Figure 13; Lister, 1977). Analysis of the quartz CPO by EBSD reveals that recrystallization was accommodated mostly by prism <a> and minor rhomb <a> slip (Schmidt and Casey, 1986) across all textures – from proto- to ultra-mylonite. Proto- and meso-mylonite seem to have slightly greater contribution of rhomb <a> slip compared to the ultramylonitic samples (Figure 13). However, the dominance of prism <a> slip suggests that the temperature of deformation was above 500°C, which is consistent with our optical observations of grain boundary migration recrystallization in quartz and limited subgrain rotation recrystallization in feldspar (e.g. Schmid and Casey, 1986; Stipp et al., 2002; Passchier and Trouw, 2005). The c-axis girdle is narrow and typically displays a central bullseye associated with the prism <a> slip. The rhomb <a> contribution to the c-axis polefigure gives a slight dextral asymmetry to the gridle consistent with a top-to-the-southwest sense of shear in the proto- and meso-mylonitic samples. The ultra-mylonitic c-axis polefigure is nearly symmetrical. These observations suggest that the SRMZ experienced nearly coaxial component of deformation (Passchier and Trouw, 2005; Barth et al., 2010).

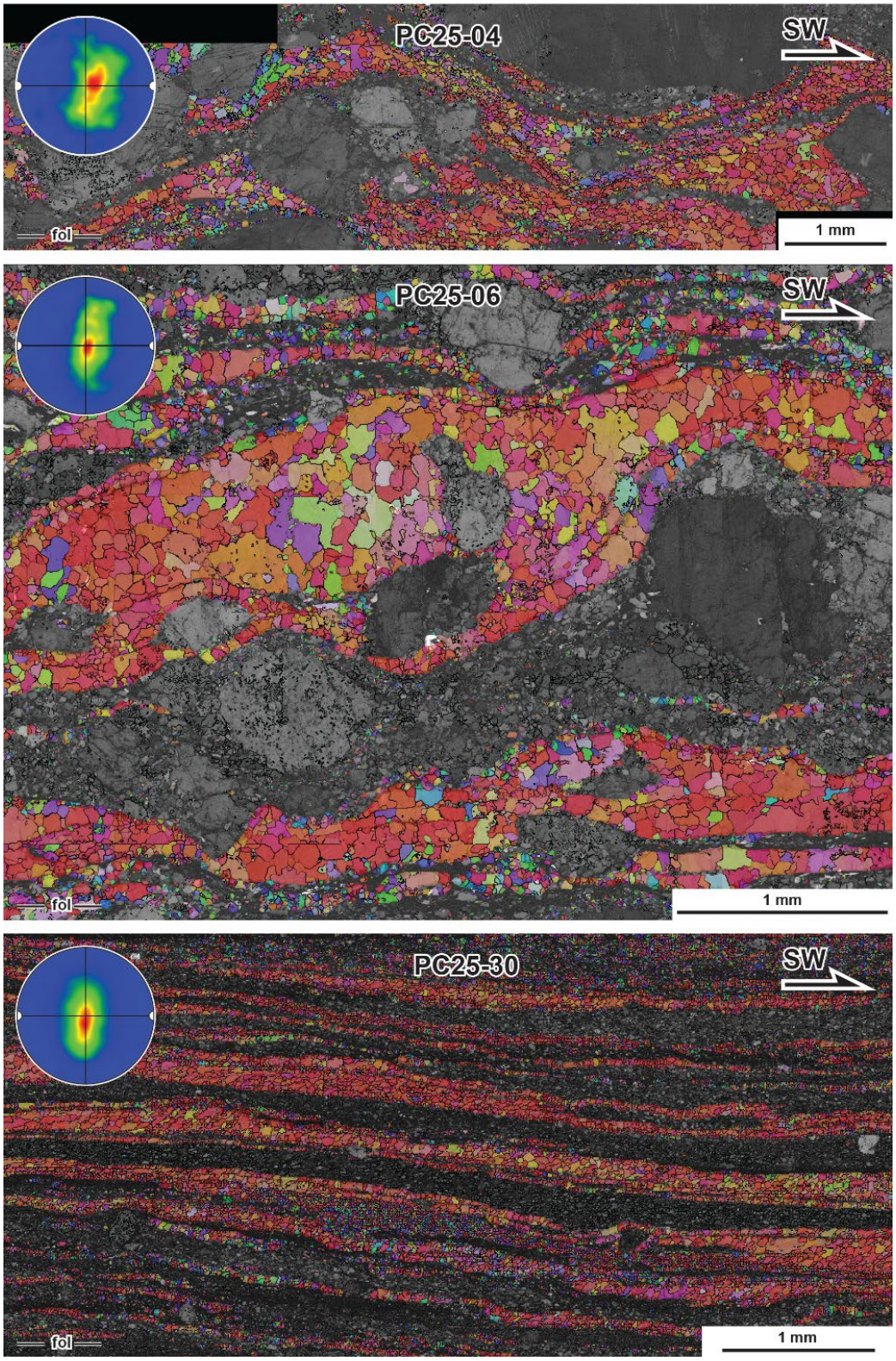

Figure 13: Detailed EBSD grain maps for proto- (PC25-04), meso- (PC25-06), and ultra- (PC25-30) mylonite samples. Quartz grains are shown in random colors overlaid on the band contrast image. Black lines are grain boundaries. Each image contains a quartz c-axis polefigure for the samples. Samples oriented perpendicular to the foliation and parallel to the lineation, with a top right to the southwest sense of shear.

5. Discussion

We have focused on the different parameters that may have influenced strain localization in the SRMZ. Much of the previous research has focused on the regional anisotropies of geologic relationships, and specifically elucidating the timing of deformation, from emplacement of the PRB to timing of emplacement and thrusting of the Asbestos Mountain granodiorite (Erskine and Wenk, 1985; Wenk, 1998; Goodwin and Renne, 1991, Wenk et al., 2000). The SRMZ is localized at the contact between granodioritic intrusions and likely initiated within the PRB (Goodwin and Wenk, 1995). However, the reason for such heterogeneous strain distribution remains challenging. In this discussion we highlight the role of original mineralogy in strain localization and accommodation processes and provide prospective on events in the SRMZ.

5.1. Strain Localization in the Santa Rosa Mylonite Zone

We recall strain localization as the response a rock has to stress based on its grain size, mineral composition, fluid interaction, mechanical anisotropies, and pre-existing weaknesses (e.g., Fossen and Cavalcante, 2017; Corvò et al., 2022; Li and Cao, 2025). It is typically expressed by grain size reduction, concentration of weak minerals, and crystallographic preferred orientations. Regionally, structurally mechanic anisotropies can significantly influence strain localization (Pennacchio and Mancktelow, 2007; Fossen and Cavalcante, 2017; Li and Cao, 2025). Goodwin and Wenk (1995) suggested the SRMZ developed from initial grain size reduction with brittle deformation (cataclasis) followed by ductile flow, forming phyllonites (see also Section 5.3.). Our observations, from field relations to hand sample variability, to thin sections (Figures 7-9), suggest that strain is heterogeneously distributed at all scales, which is difficult to reconcile with this model. Our ultramylonitic samples systematically show greater amount of quartz and biotite than the proto- and mesomylonite (Figures 7-9). Ultramylonites also exhibit continuous layers of quartz and biotite, whereas protomylonites show patches or swaths of quartz between large feldspar porphyroclasts. We suspect in the protomylonite, because the feldspar content is higher than in the ultramylonite, the grains interact with each other, forming a load-bearing framework (Handy, 1990).

5.1.1. Role of mineral composition on deformation mechanisms

The microstructural analysis suggests that the dominant deformation mechanisms for quartz, feldspar, and biotite were the same across all textures (Figures 7-9). Samples with a higher amount of quartz and biotite exhibit greater amounts of strain localization; finely recrystallized quartz and feldspar are widely intermixed and distributed throughout the samples.

Micro- chemical and structural results suggest that all of the samples collected were derived from the same protolith, regardless of their degree of mylonitization (proto-, meso-, or ultra-mylonitic). This is supported by the EDS results (Figures 10-12) which indicate that the composition of our samples matches the mineral assemblage of a granodioritic protolith (the Eastern Peninsular Ranges Batholith). Therefore, we suggest that primary mineral distribution may play a significant role in strain localization. Indeed, the overall strength or rheology of a rock aggregate depends on the abundance of each phase, phase distribution, and phase strength contrast, and active deformation mechanisms in each phase, all of which can change with variations in pressure, temperature, stress, strain rate, and increasing strain (Handy 1990, 1994, Holyoke and Tullis, 2006; Tokle et al., 2023). Deformation conditions recorded in quartz microstructures are consistent with deformation conditions interpreted from feldspar microstructures.

5.1.2. Deformation mechanisms on temperature and viscosity

Microstructural analysis of all observed textures (from proto- to ultramylonitic) indicates that quartz is nearly entirely recrystallized and deformed primarily by grain boundary migration (Figures 7-9), indicative of deformation temperatures of 500-550°C (Regime III of Hirth and Tullis, 1992; Stipp et al., 2002, 2010). Feldspar porphyroclasts exhibited brittle (fracturing) and ductile deformation (recrystallization) suggesting deformation conditions of 450°C to 600°C (e.g., Passchier and Trouw, 2005). Together, quartz and feldspar microstructures constrain deformation temperature greater than 500°C. At such temperature, quartz is significantly less viscous than feldspar, therefore feldspar porphyroclast abundance controls the bulk strength of the aggregate. Minor variation in quartz vs. feldspar content in the starting aggregate will then lead to different mechanical responses at the same temperature and stress; a quartz rich sample will be less viscous and therefore deform at a much higher strain rate than a feldspar rich aggregate that would be more viscous in comparison. This viscosity contrast would only be enhanced with the addition of biotite, which is inherently a very weak mineral. This means the

strain distribution is largely dependent on the viscosity of feldspar when it is present. Hence, in the ultramylonite, with a lower feldspar content, porphyroclasts are scattered far apart and are small enough so that a load bearing framework cannot be developed. Thus, strain is distributed across the aggregate, deforming at the bulk viscosity of aggregate, which would be less than the viscosity of feldspar.

5.2. Strain accommodation mechanisms in the Santa Rosa mylonite zone

5.2.1. Quartz and feldspar

Petrographic analysis indicates quartz deformation by dislocation creep was primarily accommodated by grain boundary migration, suggesting deformation temperatures of 500-550°C (Regime III of Hirth and Tullis, 1992; Stipp et al., 2002, 2010). EBSD data of quartz CPOs (Figure 13) reveal that recrystallization was accommodated mostly by prism <a> and minor rhomb <a> slip (Schmidt and Casey, 1986) across all textures – from proto- to ultra-mylonite. The dominance of prism <a> slip suggests that the temperature of deformation was above 500°C (e.g. Schmid and Casey, 1986; Stipp et al., 2002; Passchier and Trouw, 2005). Large feldspar porphyroclasts exhibit both bookshelf brittle fracturing along cleavage planes, as well as recrystallization along grain boundaries, forming core-mantle structures. Pressure shadows of feldspar porphyroclasts commonly contain fine-grained recrystallized feldspar with relatively uniform grain size and polygonal grains. These feldspar microstructures suggest deformation conditions of 450°C to 600°C (e.g., Passchier and Trouw, 2005). The dominance of grain boundary migration in quartz, combined with prism <a> slip observed in c-axis polefigure, and feldspar recrystallization, suggest a minimum temperature of deformation for the SRMZ of 500°C.

5.2.2. Biotite

Strain likely preferentially localized in biotite rich layers, since biotite is mechanically weak due to its ability to slip on its basal plane. With progressive strain accumulation, these biotite rich layers completely recrystallized, forming this very fine grain ultramylonite. This strain accommodation mechanism seems to be common across all our ultramylonitic samples, because as noted in Section 5.1., they all contain a greater modal amount of biotite than in the protomylonitic samples.

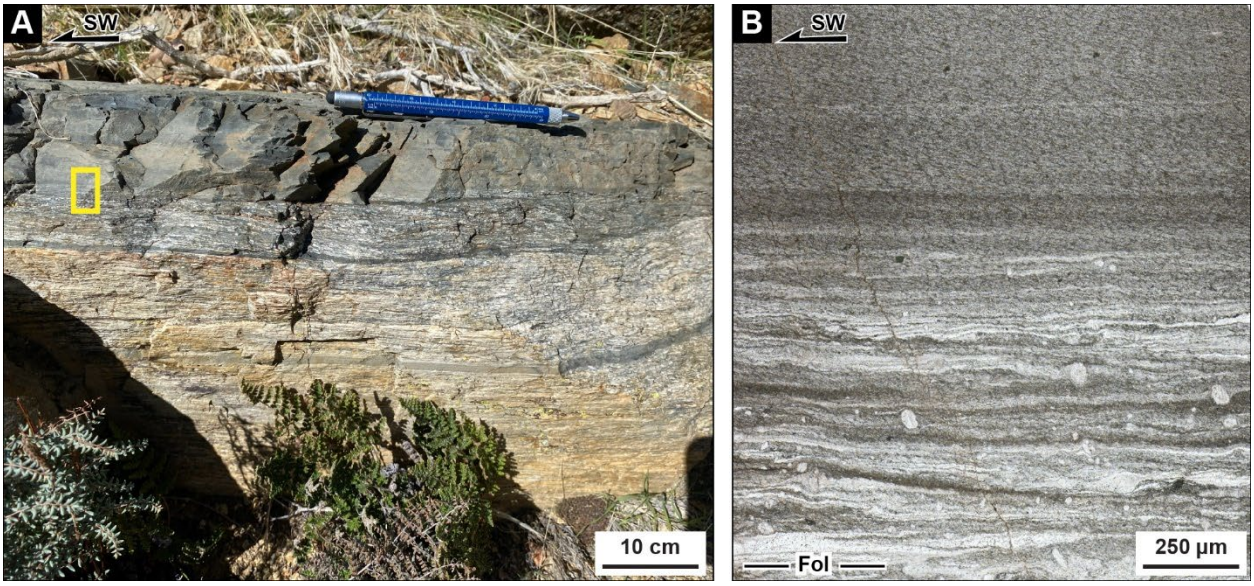

Figure 14: (A) Example of "phyllonite" found along transect at Location 2. Yellow box indicates area sampled [PC25-28] for thin section (B). Thin section shows that the matte, dark, material consist primarily of recrystallized biotite.

5.3. Phyllonites

The two structural transects conducted in this study are located within the same area as the Goodwin and Wenk (1995) study. Along our transect (Figure 4), we observed several 2-20 cm thick layers of dark, matte material with strong foliation (Figure 14). Samples collected from these lithologies indicate that they are primarily composed of finely recrystallized biotite grain, that define the S-C fabric of the rock. The texture of the rocks immediately adjacent to these darker layers is ultramylonitic (Figure 14), characterized by significant recrystallization and grain size reduction, with only a few feldspar porphyroclasts. Thinner layers of recrystallized biotite are commonly found in the field, and throughout our ultramylonitic samples (Figure 7). We therefore suggest that they represent part of the ultramylonite rather than a separate unit of phyllonite.

5.4. Implications for Exhumation

The evolution of the SRMZ has previously been constrained by thermochronological data (Figure 15). Cooling paths suggests that deformation of the SRMZ occurred after the emplacement of the PRB (inferred intrusion age for the granodiorite is ~97 Ma, Hill and Silver), and during and after the emplacement and thrusting of the Asbestos Mountain granodiorite in

($^{40}Ar/^{39}Ar$ age of ~62 Ma, Goodwin and Renne, 1991, Wenk et al., 2000) over a period of 20 million years (Goodwin and Renne, 1991).

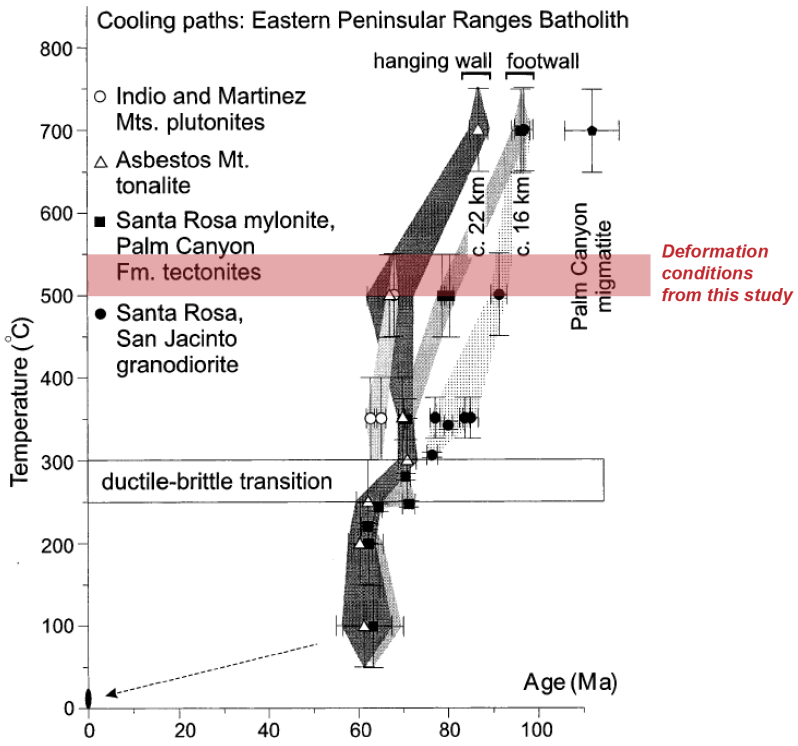

Figure 15: Cooling curves from the footwall and hanging wall of the SRMZ, compilation from Wenk et al. (2000). Fission track, 40Ar/39Ar, K/Ar, and U/Pb mineral ages from Armstrong and Suppe (1973), Hill and Silver (1980), Dokka (1984), Cecil (1990; unpublished), Goodwin and Renne (1991). Ages are plotted against the estimated average or calculated closure temperatures for the different isotopic systems.

5.4.1. Thermochronological evolution

The microstructural results presented in our study lack any deformation microstructure indicative of temperature below 500°C and equally lack any evidence of predominantly brittle deformation in the SRMZ. In addition, the fact that quartz is almost entirely recrystallized suggests that the SRMZ must have evolved at temperature >500°C for a considerable amount of time for such microstructures to develop. Wenk et al. (2000) suggest that by ~70 Ma, both the hanging wall and footwall of the SRMZ had cooled to <300°C, implying that major ductile deformation had terminated at that time. If that is the case, then the observed microstructures must be associated with the early, high temperature deformation of the SRMZ, prior to 70 Ma. Consequently, we suspect this deformation to be associated with the emplacement of the batholith rather than the thrusting of the Asbestos Mountain granodiorite.

5.4.2. Kinematic analysis of quartz on major deformation component

CPOs of quartz c-axis polefigures from the ultramylonite are nearly symmetrical, and polefigures from the proto- and meso-mylonite show a slight dextral asymmetry consistent with a top-to-the-southwest sense of shear. These observations suggest that the SRMZ dominantly experienced a coaxial component of deformation, i.e., mostly pure shear or flattening (Passchier and Trouw, 2005; Barth et al., 2010). This is consistent with Wenk's 1998 findings of finite strain analysis of xenoliths found in the SRMZ, which shows mostly flattening strain produced during emplacement of the partially solidified batholith.

6. Conclusions

This study of the Santa Rosa mylonite zone demonstrates that strain localization in polymineralic rocks is fundamentally controlled by primary mineralogical heterogeneity, even under relatively uniform deformation conditions. Integrated microstructural, microchemical, and EBSD analyses show that quartz accommodated deformation predominantly by grain boundary migration at temperatures exceeding ~500 °C, while feldspar exhibited mixed brittle–ductile behavior and biotite formed interconnected weak layers that defined the mylonitic fabric. Although deformation mechanisms are broadly consistent across proto-, meso-, and ultra- mylonitic samples, systematic variations in modal mineralogy strongly influence strain distribution. Quartz- and biotite-rich domains promote strain localization through reduced aggregate strength and enhanced phase connectivity, whereas feldspar-rich domains maintain a load-bearing framework that inhibits localization. These findings highlight the critical role of phase proportions and spatial distribution in governing the rheological evolution of shear zones and suggest that even subtle variations in initial mineral assemblage can lead to significant heterogeneity in strain accommodation during mid-crustal deformation.

References

Alaoui, K., Airaghi, L., Dubacq, B., Rosenberg, C.L., Bellahsen, N., and Précigout, J., 2023, Role of pre-kinematic fluid-rock interactions on phase mixing, quartz recrystallization and strain localization in low-temperature granitic shear zones: Tectonophysics, v. 850, no. 5, 17 p., doi:10.1016/j.tecto.2023.229735.

Armstrong, R.L., Suppe, J., 1973. Potassium-argon geochronometry of Mesozoic igneous rocks in Nevada, Utah and southern California: Geological Society of America Bulletin, v. 84, p. 1375-1392.

Axen, G.J., van Wijk, J.W., Currie, C.A., 2018, Basal continental mantle lithosphere displaced by flat-slab subduction: Nature Geoscience, v. 11, p. 961–964, doi:10.1038/s41561-018-0263-9.

Bui, D.V., Takeshita, T., Ando, J., Yamamoto, T., Huang, W., Yeo, T., and Czertowicz, T.A., 2023, Development of the Median Tectonic Line-related shear zone, southwest Japan: An analysis of strain localization processes: Tectonophysics, v. 850, no. 5, 17 p., doi:10.1016/j.tecto.2023.229751.

Carreras, J., 2001, Zooming on Northern Cap de Creus shear zones: Journal of Structural Geology, v. 23, p. 1457-1486, doi:10.1016/S0191-8141(01)00011-6.

Carreras, J., Czeck, D.M., Druguet, E., and Hudleston, P.J., 2010, Structure and development of an anastomosing network of ductile shear zones: Journal of Structural Geology, v. 32, p. 656-666, doi:10.1016/j.jsg.2010.03.013.

Corvò, S., Maino, M., Piazolo, S., Seno, S., and Langone, A. (2022). Role of inherited compositional and structural heterogeneity in shear zone development at mid-low levels of the continental crust (the Anzola shear zone; Ivrea-Verbano Zone, Southern Alps). Lithos, 422, 106745.

Cross, A. J., Prior, D. J., Stipp, M., and Kidder, S., 2017, The recrystallized grain size piezometer for quartz: An EBSD-based calibration: Geophysical Research Letters, v. 44, no. 13, p. 6667-6674, doi:10.1002/2017GL073836.

Dokka, R.K., 1984, Fission-track geochronological evidence for late Cretaceous mylonitization and early Paleocene uplift of the northeastern Peninsular Ranges, California: Geophysical Research Letters, v. 11, p. 46-49, doi:10.1029/GL011i001p00046.

Erskine, B.G., and Wenk, H.-R., 1985, Evidence for Late Cretaceous crustal thinning in the Santa Rosa mylonite zone, southern California: Geology, v. 13, p. 274-277.

Ferré, E. C., Geissman, J. W., and Zechmeister, M. S. (2012). Magnetic properties of fault pseudotachylytes in granites. Journal of Geophysical Research: Solid Earth, 117(B1).

Fossen, H., Cavalcante, G.C.G, 2017, Shear zones – A review, Earth-Science Reviews, v.171 p.434-455, doi:10.1016/j.earscirev.2017.05.002.

Gardner, R., Piazolo, S., Evans, L., and Daczko, N., 2017, Patterns of strain localization in heterogeneous, polycrystalline rocks – a numerical perspective: Earth and Planetary Science Letters, v. 463, p. 253-265, doi:10.1016/j.epsl.2017.01.039.

Goodwin, L. B., and Renne, P. R., 1991, Effects of progressive mylonitization on Ar retention in biotites from the Santa Rosa mylonite zone, California, and thermochronologic implications: Contributions to Mineralogy and Petrology, v. 108, p. 283-297, doi:10.1007/BF00285937.

Goodwin, L. B., and Tikoff, B., 2002, Competency contrast, kinematics, and the development of foliations and lineations in the crust: Journal of Structural Geology, v. 24, p. 1065- 1085, doi:10.1016/S0191-8141(01)00092-X.

Handy, M. R., 1990, The solid-state flow of polymineralic rocks. Journal of Geophysical Research: Solid Earth, v. 95, no. B6, p. 8647-8661.

Handy, M. R., 1994, Flow laws for rocks containing two non-linear viscous phases: a phenomenological approach: Journal of Structural Geology, v. 16, no. 3, p. 287-301.

Hill, R.I., Silver, L.T., 1980, Strontium isotopic variability in the pluton of San Jacinto Peak, southern California, EOS, Trans. Am. Geophys. Union 61:411.

Hirth, G., Teyssier, C., and Dunlap, J.W., 2001, An evaluation of quartzite flow laws based on comparisons between experimentally and naturally deformed rocks: International Journal of Earth Sciences, v. 90, no. 1, p. 77-87, doi:10.1007/s005310000152.

Holyoke III, C. W., and Tullis, J., 2006, Mechanisms of weak phase interconnection and the effects of phase strength contrast on fabric development: Journal of Structural Geology, v. 28, no. 4, p. 621-640.

Jefferies, S. P., Holdsworth, R. E., Wibberley, C. A. J., Shimamoto, T., Spiers, C. J., Niemeijer, A. R., and Lloyd, G. E., 2006, The nature and importance of phyllonite development in crustal-scale fault cores: an example from the Median Tectonic Line, Japan: Journal of Structural Geology, v. 28, no. 2, p. 220-235.

Jiang, H., Lee, C-T.A., Morgan, J.K., and Ross, C.H., 2015, Geochemistry and thermodynamics of an earthquake: A case study of pseudotachylites within mylonitic granitoid: Earth and Planetary Science Letters, v. 430, p. 235-248, doi:10.1016/j.epsl.2015.08.027.

Johnston, K.L., Goodwin, L., Tikoff, B., Earnest, E., Gopon, C., Blenkinsop, T.G., 2025, Naturally deformed polymineralic rocks provide quantitative rheological information: Journal of Structural Geology, doi.org/10.1016/j.jsg.2025.105539.

Jones, A.D., Wright, E.V., House, M.A., Heap, C.I., Newton, S., Brooks, D.A., and Skinner, S., 2025, Geology of California, Academic Senate of California Community Colleges Open Educational Resource Initiative.

Klepeis, K.A., Schwartz, J.J., Miranda, E.A., Baskin, J., Mendez, A.C., and Mora-Klepeis, G., 2025, Influence of magmatism on the architecture of transpressional faults and shear zones in the deep crust of the Late Cretaceous Southern California batholith: Geological Society of America Bulletin, 25 p., doi:10.1130/B38219.1.

Kohlstedt, D.L., Evans, B., and Mackwell, S.J., 1995, Strength of the lithosphere: Constraints imposed by laboratory experiments: Journal of Geophysical Research, v. 100, p. 17587-17602, doi:10.1029/95JB01460.

Knoph, E.B., 1931, Retrogressive Metamorphism and Phyllonitization: American Journal of Science, v. 21.

Li, J., and Cao, S., 2025, Strain Localization and Seismic Properties in the Heterogeneous Ailaoshan-Red River Shear Zone, Southeast Asia: Geochemistry, Geophysics, Geosystems, v. 26, 25 p., doi:10.1029/2024GC011929.

O'Brien, D.K., Wenk, H.-R., Ratschbacher, L., and You, Z., 1987, Preferred orientation of phyllonites and ultramylonites: Journal of Structural Geology, v. 9, p. 719-730, doi:10.1016/0191-8141(87)90155-6.

Passchier, C.W., and Trouw, R.A.J., 2005, Microtectonics: Berlin, Springer, 366 p., doi: 10.1007/3-540-29359-0.

Pennacchioni, G., and Mancktelow, N. S., 2007, Nucleation and initial growth of a shear zone network within compositionally and structurally heterogeneous granitoids under amphibolite facies conditions: Journal of Structural Geology, v. 29, no. 11, p. 1757-1780.

Rowe, C. D., Kirkpatrick, J. D., and Brodsky, E. E., 2012, Fault rock injections record paleo-earthquakes. Earth and Planetary Science Letters, v. 335, p. 154-166.

Secchi, M., Zanatta, M., Borovin, E., Bortolotti, M., Kumar, A., Giarola, M., Sanson, A., Orberger, B., Daldosso, N., Gialanella, S., Mariotto, G., Montagna, M., and Lutterotti, L., 2018, Mineralogical investigations using XRD, XRF, and Raman spectroscopy in combined approach: Special Issue-Research Article, doi:10.1002/jrs.5386.

Shea, W.T., Jr., and Kronenberg, A.K., 1993, Strength and anisotropy of foliated rocks with varied mica contents: Journal of Structural Geology, v. 15, p. 1097-1121, doi:10.1016/0191-8141(93)90158-7.

Simpson, C., 1984, Borrego Springs-Santa Rosa mylonite zone: A Late Cretaceous west-directed thrust in southern California: Geology, v. 12, p. 8-11.

Stipp, M., Stünitz, H., Heilbronner, R., and Schmid, S.M., 2002, The eastern Tonale fault zone: a 'natural laboratory' for crystal plastic deformation of quartz over a temperature range from 250 to 700 °C: Journal of Structural Geology, v. 24, p. 1861-1884, doi:10.1016/S0191-8141(02)00035-4.

Stipp, M., Stunitz, H., Heilbronner, R., and Schmid, S. M., 2002, The eastern Tonale fault zone: a 'natural laboratory'for crystal plastic deformation of quartz over a temperature range from 250 to 700 C: Journal of structural geology, v. 24, no. 12, p.1861-1884.

Stipp, M., and Tullis, J., 2003. The recrystallized grain size piezometer for quartz. Geophysical Research Letters, v. 30, no. 21, doi:10.1029/2003GL018444.

Stipp, M., Tullis, J., Scherwath, M., and Behrmann, J. H., 2010, A new perspective on paleopiezometry: Dynamically recrystallized grain size distributions indicate mechanism changes. Geology, v. 38 no. 8, p. 759-762.

Tokle, L., Hirth, G., and Stünitz, H., 2023, The effect of muscovite on the microstructural evolution and rheology of quartzite in general shear: Journal of Structural Geology, v. 169, 104835, doi:10.1016/j.jsg.2023.104835.

Tullis, J., and Wenk, H.-R., 1994, Effect of muscovite on the strength and lattice preferred orientations of experimentally deformed quartz aggregates: Materials Science and Engineering, v. 175, p. 209-220, doi:10.1016/0921-5093(94)91060-X.

Wenk, H.-R., Johnson, L.R., and Ratschbacher, L., 2000, Pseudotachylites in the Eastern Peninsular Ranges of California: Tectonophysics, v. 321, no. 2, p. 253-277.

Wenk, H.R., and Pannetier, J., 1990, Texture development in deformed granodiorites from the Santa Rosa mylonite zone, southern California. Journal of Structural Geology, v. 12, p. 177-184, doi:10.1016/0191-8141(90)90003-H.

Wenk, H.R., 1998, Deformation of mylonites in Palm Canyon, California, based on xenolith geometry. Journal of Structural Geology, v. 20, p. 559-571, doi:10.1016/S0191-8141(97)00114-4.

Yonkee, W.A., and Weil, A.B., 2015, Tectonic evolution of the Sevier and Laramide belts within the North American Cordillera orogenic system: Earth-Science Reviews, v. 150, p. 531-593, doi:10.1016/j.earscirev.2015.08.001.